

Velocity and Temperature Structure Functions in the Upper Troposphere and Lower Stratosphere from High-Resolution Aircraft Measurements

DONALD E. WROBLEWSKI

Mechanical Engineering Department, Boston University, Boston, Massachusetts

OWEN R. COTÉ

Air Force Research Laboratory, Hanscom AFB, Bedford, Massachusetts

JORG M. HACKER

Flinders University, Adelaide, South Australia, Australia

RONALD J. DOBOSY

NOAA/ARL, Oak Ridge, Tennessee

(Manuscript received 17 February 2009, in final form 16 October 2009)

ABSTRACT

High-resolution measurements obtained from NOAA “best” atmospheric turbulence (BAT) probes mounted on an EGRETT high-altitude research aircraft were used to characterize turbulence in the upper troposphere and lower stratosphere at scales from 2 m to 20 km, focusing on three-dimensional behavior in the sub-kilometer-scale range. Data were analyzed for 129 separate level flight segments representing 41 h of flight time and 12 600 km of wind-relative flight distances. The majority of flights occurred near the tropopause layer of the winter subtropical jet stream in the Southern Hemisphere. Second-order structure functions for velocity and temperature were analyzed for the separate level-flight segments, individually and in various ensembles. A 3D scaling range was observed at scales less than about 100 m, with power-law exponents for the structure functions of the velocity component in the flight direction varying mostly between 0.4 and 0.75 for the separate flight segments, but close to $2/3$ for the ensemble-averaged curves for all levels and for various sub-ensembles. Structure functions in the 3D scaling range were decoupled from those at scales greater than 10 km, with the large-scale structure functions showing less variation than those at smaller scales. Weakly anisotropic behavior was observed in the 3D range, with structure parameters for the lateral and vertical velocities on the same order as those in the flight direction but deviating from the expected isotropic value. Anisotropy was correlated with turbulence intensity, with greater anisotropy associated with weaker turbulence.

1. Introduction

Turbulence in the upper troposphere and lower stratosphere (UTLS) can adversely impact the performance of a range of aerospace systems. Optical turbulence (OpT) from fluctuations in temperature and humidity can affect electromagnetic propagation, disrupting communications, radar, high-energy laser systems, and space imaging.

Similarly, clear-air turbulence (CAT) can lead to aircraft upset, a problem particularly acute for stratospheric vehicles that often must fly within a narrow flight envelope. Thus, reliable prediction is critical for turbulence avoidance and mitigation in these operational situations. Unfortunately, prediction is difficult because of the nature of UTLS turbulence, which is concentrated in very thin layers with thicknesses of hundreds of meters to a few kilometers, a scale smaller than the typical resolution of mesoscale weather forecasting models. As such, prediction and forecasting rely on parameterized models, based on statistical correlations and phenomenological relations between mesoscale parameters and turbulence

Corresponding author address: Donald E. Wroblewski, Mechanical Engineering Dept., Boston University, 110 Cummington St., Boston, MA 02482.
E-mail: dew11@bu.edu

Report Documentation Page

Form Approved
OMB No. 0704-0188

Public reporting burden for the collection of information is estimated to average 1 hour per response, including the time for reviewing instructions, searching existing data sources, gathering and maintaining the data needed, and completing and reviewing the collection of information. Send comments regarding this burden estimate or any other aspect of this collection of information, including suggestions for reducing this burden, to Washington Headquarters Services, Directorate for Information Operations and Reports, 1215 Jefferson Davis Highway, Suite 1204, Arlington VA 22202-4302. Respondents should be aware that notwithstanding any other provision of law, no person shall be subject to a penalty for failing to comply with a collection of information if it does not display a currently valid OMB control number.

1. REPORT DATE APR 2010		2. REPORT TYPE		3. DATES COVERED 00-00-2010 to 00-00-2010	
4. TITLE AND SUBTITLE Velocity and Temperature Structure Functions in the Upper Troposphere and Lower Stratosphere From High-Resolution Aircraft Measurements				5a. CONTRACT NUMBER	
				5b. GRANT NUMBER	
				5c. PROGRAM ELEMENT NUMBER	
6. AUTHOR(S)				5d. PROJECT NUMBER	
				5e. TASK NUMBER	
				5f. WORK UNIT NUMBER	
7. PERFORMING ORGANIZATION NAME(S) AND ADDRESS(ES) Mechanical Engineering Department, Boston University, Boston, MA				8. PERFORMING ORGANIZATION REPORT NUMBER	
9. SPONSORING/MONITORING AGENCY NAME(S) AND ADDRESS(ES)				10. SPONSOR/MONITOR'S ACRONYM(S)	
				11. SPONSOR/MONITOR'S REPORT NUMBER(S)	
12. DISTRIBUTION/AVAILABILITY STATEMENT Approved for public release; distribution unlimited					
13. SUPPLEMENTARY NOTES					
14. ABSTRACT We report a systematic measurement of the space charge effect observed in the few-ps laser pulse regime in laser-based solid-state photoemission spectroscopy experiments. The broadening and the shift of a gold Fermi edge as a function of spot size, laser power, and emission angle are characterized for pulse lengths of 6 ps and 6 eV photon energy. The results are used as a benchmark for an N-body numerical simulation and are compared to different regimes used in photoemission spectroscopy. These results provide an important reference for the design of time and angle-resolved photoemission spectroscopy setups and next-generation light sources.					
15. SUBJECT TERMS					
16. SECURITY CLASSIFICATION OF:			17. LIMITATION OF ABSTRACT	18. NUMBER OF PAGES	19a. NAME OF RESPONSIBLE PERSON
a. REPORT unclassified	b. ABSTRACT unclassified	c. THIS PAGE unclassified			

quantities, in order to identify regions that have the potential for high levels of clear air or optical turbulence. These approaches are only as good as the fundamental understanding of UTLS turbulence structure that forms the underlying foundation for the models; such insight must be gleaned from experimental data, detailed microscale simulations, highly nested mesoscale model runs, or a combination of all three.

Two seminal experiments have formed the primary database for studying UTLS turbulence, both involving instrumentation of commercial transport aircraft. The Global Atmospheric Sampling Project (GASP) utilized specially selected Boeing 747 in routine commercial airline service from 1975 to 1979, representing 6900 flights, instrumented to measure horizontal wind velocity, temperature, and trace constituents (Perkins 1976; Nastrom and Jasperson 1983). A summary of the GASP dataset can be found in Jasperson et al. (1990) and Nastrom and Gage (1985). The Measurement of Ozone and Water Vapor by Airbus In-Service Aircraft (MOZAIC) project utilized five specially instrumented Airbus aircraft in normal commercial operation from 1994 to 1997, representing over 7500 flights and 54 000 flight hours (Marengo et al. 1998). Although the major emphasis of the program was water vapor and ozone measurements, meteorological data included horizontal wind velocity and temperature, with data sampling at 4-s intervals on all flights.

The wealth of data from these two campaigns, and the reinterpretation of the data by Lovejoy et al. (2009) and Lilley et al. (2008), has furthered the understanding of UTLS turbulence; however, spatial resolution was limited due to sampling rates and the speed of the aircraft, restricting investigation of turbulence structure and phenomena to larger scales—from a few kilometers up to thousands of kilometers. Unfortunately, this range of scales does not encompass the key features of CAT or OpT, both of which are characterized by scales in the 1 m to 1 km range and are associated with three-dimensional phenomena that cannot be investigated using only horizontal velocities (e.g., the vertical velocity, which is a critical contributor to aircraft response to CAT).

Although aircraft data at scales down to about 80 m are available from other aircraft campaigns, these are associated with limited numbers of reported flight segments (e.g., Kennedy and Shapiro 1980; Chan et al. 1998).

One solution to the scale problem has been to extrapolate large-scale experimental or mesoscale model data to microscale behavior. Lindborg (1999, hereafter L99) and Cho and Lindborg (2001, hereafter CL01) estimated dissipation from MOZAIC data by fitting structure functions and assuming two-dimensional turbulence behavior. Frehlich and Sharman (2005, hereafter FS05) used the curve fits from L99 to extrapolate mesoscale model

results to smaller scales for estimating dissipation, structure functions, and other characteristics of microscale turbulence. However, these methods have not been verified because of the dearth of available data at small scales, as pointed out in FS05. This paper will show that such extrapolations are not universally valid.

The work presented in this paper aims to fill the gap in published UTLS experimental data for turbulence of scales in the range from approximately 1 m to 1 km. The work focuses on analysis of structure functions calculated using high-resolution turbulence measurements of temperature and all three components of velocity as part of a multiyear effort (1998–2006) to study CAT and OpT. The overall objective is to probe the small-scale structure of UTLS turbulence in the hopes of furthering our understanding of atmospheric phenomenon in general and of providing data for building and testing more effective parameterized models for prediction and forecasting.

2. Measurements

Aircraft measurements were acquired with the Grob 520T EGRETT aircraft, the sole twin-seat version of the four Grob 520 aircraft produced, which was operated by Airborne Research of Australia of Flinders University. This high-altitude, turboprop research aircraft is capable of operation at altitudes up to 15 km at air speeds of approximately 100 m s^{-1} with an endurance of 8 h. The aircraft can accommodate up to three National Oceanic and Atmospheric Administration (NOAA)-built “best” atmospheric turbulence (BAT) probes (Crawford and Dobosy 1992, 1997), one located under each wing and one at the top of the tail. The structure functions obtained from the two underwing probes were, in general, nearly identical, so the left BAT probe was used for analysis, except in cases when its signal was noisier than that from the right probe or for the occasional flights when data were missing or out of range. The tail probe data were not used in this study.

The BAT probe has a 13-cm-diameter hemisphere with nine pressure ports for measurement of all three components of wind velocity and a microbead thermistor located inside the central dynamic pressure port for temperature measurement. Beginning in 2002, the NOAA Fast Ultrasensitive Temperature (FUST) probe was also mounted externally on the top of the BAT probe body. This bare-wire microthermocouple sensor featured increased signal-to-noise compared to the thermistor, so its output was used when available. For three of the campaigns (described below), the right-wing BAT probe was replaced with a standard Rosemont five-hole probe with a Rosemont PT50 probe for temperature.

Wind velocities were obtained by subtracting pressure-sphere-derived, wind-relative aircraft velocity measurements from the ground-fixed aircraft velocities and orientations (pitch, yaw, and roll) obtained from the Inertial Navigation System (INS) and GPS measurements. With this approach, vertical wind velocity is most prone to error, since it is found by subtracting two numbers that are nearly equal to obtain a small number, and because it is more sensitive to aircraft angle of attack than the horizontal wind velocities. Garman et al. (2006) found a 1σ precision of 0.03 m s^{-1} for the vertical velocity measured with the BAT probe after being calibrated in a wind tunnel. However, without such calibration, the overall error in the wind components is closer to 0.25 m s^{-1} (Crawford and Dobosy 1992). For comparison, Nastrom et al. (1984) report an overall accuracy of 0.5 m s^{-1} for the GASP measurements and in L99, a similar level of accuracy was reported for the MOZAIC measurements.

For nearly all flights prior to 2006, velocity and temperature data were sampled at 50, 55.6, or 58.8 Hz, providing horizontal spatial resolution of approximately 1.4 to 2 m. For 2006, the sampling rate was 10 Hz and for November 2002, it was 25 Hz, reducing spatial resolution to approximately 10 m and 4 m, respectively. Frequency response of the velocity measurements was generally near or above the sampling frequency. On the other hand, the time constant of the BAT thermistor probe resulted in a thermal lag drop-off at scales near 20 to 30 m. Both the FUST and the Rosemont temperature sensors had slightly faster response, but still exhibited drop-off in the 10- to 20-m scale range.

A typical flight featured several level flight segments at altitudes from 7 up to 14 km, covering wind-relative distances from 45 to 350 km. The EGRETT was flown on autopilot, set to maintain constant pressure altitude, with altitude variations less than $\pm 25 \text{ m}$ for all but five of the 129 flights. As a general rule, the segments were flown upwind or downwind, with over 75% of the distances flown with angles between wind and flight path of less than 30° . Approximately 5% of the flight distance involved significant crosswind components, with angles greater than 70° . Data were also available for climb and descent between level segments for some flights, and these were used to estimate vertical gradients.

Lovejoy et al. (2004, hereafter LST04) have shown that spectra and structure functions derived from airborne turbulence measurements can be strongly influenced by aircraft trajectories, an effect due to anisotropic scaling in the horizontal and vertical directions, combined with vertical excursions of the aircraft in response to the turbulence motions. This effect is seen at large scales, where aircraft inertia no longer attenuates altitude fluctuations. Following the approach in LST04, the extent of the aircraft

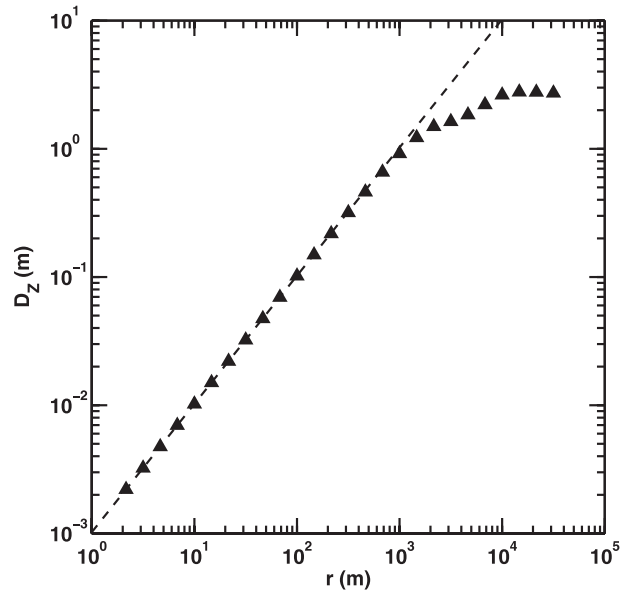


FIG. 1. First-order structure function of aircraft altitude fluctuations for 1 Sep 1998 at 13.1 km. Dashed line is $D_Z = sr$, where s is the slope of the aircraft trajectory.

inertia range was found from the first-order structure function of aircraft altitude fluctuations:

$$D_Z(r) = \langle |z_{AC}(x) - z_{AC}(x+r)| \rangle. \quad (1)$$

Note that D_Z follows a linear scaling with r in the aircraft-inertia range, estimated to be at scales less than 1 km, as seen in Fig. 1 for one of the levels. The 1-km upper limit is slightly lower than the ER-2 value of 3 km (LST04) because of the lower wing loading of the EGRETT (25 lb ft^{-2} compared to 40 lb ft^{-2}). The D_Z plots for all other cases showed aircraft-trajectory slopes on the order of 1 to 4 m km^{-1} , similar to values seen in ER-2 data (LST04) and estimates for the MOZAIC data (Lilley et al. 2008). Based on these results, quantitative analysis of structure functions will be confined to sub-kilometer scales, and interpretation of larger-scale behavior will be limited to qualitative observations. Additional discussion of the effects of aircraft trajectories on measured structure functions can be found in section 5a.

The 129 level flight segments selected for analysis are summarized in Table 1. They represent 41 h of flight time and 12 600 km of wind-relative flight distances, much less than the MOZAIC and GASP campaigns, but significant given the higher data rates and the flight planning required for targeting strong turbulence periods.

To maximize the likelihood of finding turbulence, the measurement flights were focused on the winter subtropical jet stream, primarily in and around Adelaide, Southern Australia, which was the base of operation for

TABLE 1. Summary of level flight segments (SA, South Australia; JA, Japan; WA, Wales; DA, Darwin, Australia; f_s , sampling frequency; D , total distance of level segments in wind-relative coordinates).

Dates	Loc.	No. segments	Alt (km)	f_s (Hz)	D (km)
1998: 8/25–9/03	SA	25	6.8–14.2	55.6	1900
1999: 2/03–2/21	JA	19	5.8–12.4	58.8	2026
1999: 8/6	SA	7	9.0–12.2	58.8	710
2000: 5/10–6/6	WA	20	8.1–13.8	55.6	2112
2001: 8/17–8/24	SA	15	8.5–10.8	55.6	1335
2002: 8/28–9/16	SA	37	7.1–14.0	50	4101
2002: 11/22	DA	5	9.6–14.4	25	442
2006: 8/6	SA	1	8.5	10	50

the EGRETT. Japan was the location for one of the two 1999 campaigns, with the goal of probing the strong Northern Hemisphere winter subtropical jet stream in that region. The measurements from the Adelaide and Japan flights represent 80% of the total flight distances. The remaining flights, in May and June of 2000 and in November 2002, were associated with two projects that utilized the EGRETT for primary purposes other than CAT or OpT in and near jet streams. The AberEgrett Experiment (Whiteway et al. 2003a, 2004) involved a consortium of UK researchers, and was conducted over southwest England in summer of 2000 to study gravity waves induced by the Welsh mountains and their effects on the tropospheric–stratospheric exchange of trace gases. Similarly, the EMERALD 2 (Whiteway et al. 2003b) campaign was conducted over Darwin, Australia, during the winter of 2002 to study cirrus clouds. These two campaigns employed the Rosemont probe under the right wing.

Histograms of several flight parameters, weighted based on the length of each segment in wind-relative distance, are shown in Fig. 2. The mean altitude was 10.4 km and the mean wind speed was 44.5 m s^{-1} , both exhibiting Gaussian-like distributions. The wind direction statistics reflect prevailing westerly jet streams, with a mean direction of 254° and with 84% of the flight distances within $\pm 30^\circ$ of wind from due west. The flight segment lengths exhibit a skewed distribution, with more than 75% of the flight distance flown in segments less than the mean of 123 km. The tropopause, defined here as the lowest altitude for which the lapse rate was less than 2°C km^{-1} [the World Meteorological Organization (WMO) definition], was above 11 km for all flight days and above 13 km for 85% of the flights. These high tropopause levels, found using nearby atmospheric soundings (<http://weather.uwyo.edu/upperair/sounding.html>), are not untypical for midwinter in southern Australia, resulting in 95% of the flight distances below the tropopause.

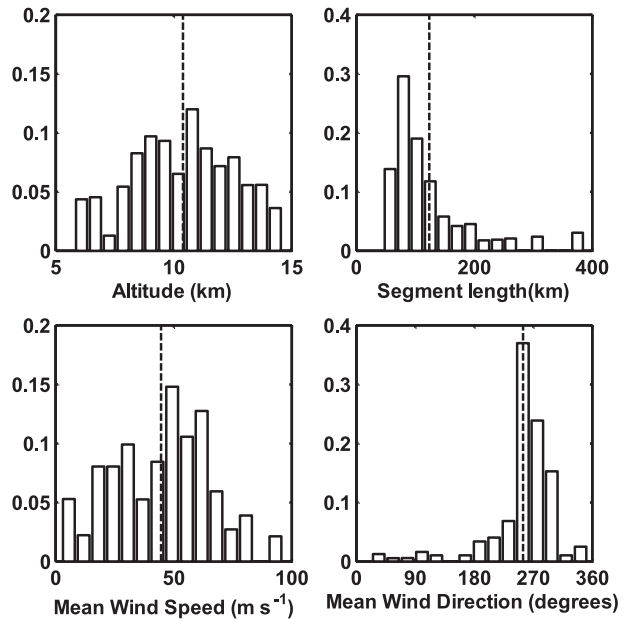


FIG. 2. Histograms showing distributions of flight parameters. Dashed lines mark mean values.

3. Structure functions

Structure functions were calculated from time series of velocity and temperature:

$$\begin{aligned}
 D_{LL}(r) &= \langle [u_L(t + r/V_{TAS}) - u_L(t)]^2 \rangle \\
 D_{NN}(r) &= \langle [u_N(t + r/V_{TAS}) - u_N(t)]^2 \rangle \\
 D_{WW}(r) &= \langle [w(t + r/V_{TAS}) - w(t)]^2 \rangle \\
 D_{TT}(r) &= \langle [T(t + r/V_{TAS}) - T(t)]^2 \rangle, \quad (2)
 \end{aligned}$$

where u_L is the component of the wind along the direction of the separation distance vector \mathbf{r} , the direction of the flight path in this case; u_N is the component normal to \mathbf{r} ; w is the vertical velocity; T is temperature; V_{TAS} is the true airspeed of the aircraft; and the angle brackets denote ensemble averaging.

Antonia and Smalley (2001) showed that structure functions generally exhibit smaller regions of power-law behavior than spectra and Nichols-Pagel et al. (2008) indicated that multitaper spectra and wavelet variances were preferred over structure functions. Despite this, structure functions provide some advantages over power spectra (L99) and thus are adopted for this study. Structure functions are often harder to interpret than spectra, lacking the direct physical interpretation of power spectra. However, structure functions are similar, though not identical, to cumulative spectra, and thus they can be interpreted in a similar manner—i.e., $D_{LL}(r)$ is a relative measure of the energy contained in $\langle u_L^2 \rangle$ for scales $\leq r$.

Equations (2) are based on a separation distance defined in wind relative coordinates, $r = V_{TAS}\Delta t$, where Δt is the time difference between data points in the measured time series. The use of wind-relative distances, which is consistent with the frozen flow hypothesis of G. I. Taylor, differs from the approach of CL01, for which latitude and longitude were used to find r in an earth-fixed coordinate frame. However, the earth-fixed approach can lead to errors with slower-flying aircraft, best illustrated by considering a case for which the aircraft is flying into a strong head wind with wind speed equal to true airspeed, such that ground speed is 0. (A similar situation occurred in 1999 during an EGRETT overwater flight south of Japan where the jet was strong enough to cause a negative ground speed.) For this zero-ground speed example, the aircraft is stationary in an earth-fixed frame, so the fixed-earth approach would erroneously lead to $r = 0$ for any two data points, regardless of the time difference. With either approach, nonstationary effects will lead to errors at large separation distances.

Structure parameters were calculated, assuming a structure-function scale range with an $r^{2/3}$ dependency:

$$C_X^2 = \frac{D_{XX}(r)}{r^{2/3}}, \quad (3)$$

where X denotes either L , N , W , or T .

Isotropic turbulence theory predicts the following relations:

$$\varepsilon = \left(\frac{C_L^2}{\alpha}\right)^{3/2}, \quad (4)$$

$$C_N^2 = C_W^2 = \frac{4}{3}C_L^2, \quad (5)$$

where ε is the dissipation rate and α is a constant, with atmospheric studies indicating a value of $\alpha \approx 2$ (Wyngaard and Coté 1971).

Average structure functions were found for each flight segment for 51 values of r , evenly spaced in logarithmic terms from 2 m to 31 km. The actual separation distances r_A for each segment varied because of differences in true airspeed and sampling rates. As such, values at the 51 specified distances were found by interpolation of the two surrounding values of r_A using a power-law fit r^n .

Scaling exponents were found for ranges of r at sub-kilometer scales that displayed linear behavior on log-log plots. This is illustrated in Fig. 3 for 25 August 1998, showing two constant slope regions demarcated by the vertical lines. For each flight segment, the linear-slope region with the exponent closest to $2/3$ for D_{LL} was used for calculating the structure parameters by force-fitting an $r^{2/3}$ curve. For example, C_L^2 is the value that minimizes the mean square error between $C_L^2 r^{2/3}$ and $D_{LL}(r)$

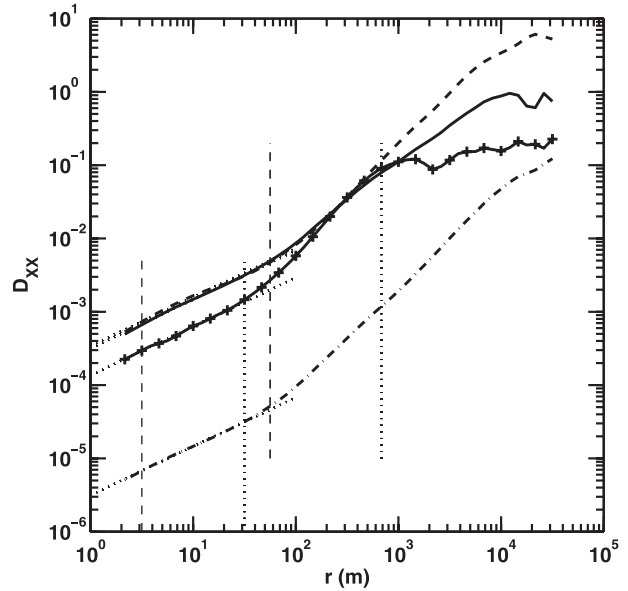


FIG. 3. Structure functions for 25 Aug 1998, 12.3 km; X refers to parameter plotted— D_{LL} ($m^2 s^{-2}$; solid line); D_{NN} ($m^2 s^{-2}$; dashed line); D_{WW} ($m^2 s^{-2}$; solid line with plus symbols); and D_{TT} (K^2 ; dotted-dashed line). Vertical dashed lines mark the beginning of constant slope regions and vertical dotted lines mark the end.

in the linear slope region. This is illustrated graphically in Fig. 3 by the dotted lines that extend from each of the structure function curves to the vertical axis, with the intercept at $r = 1$ marking the structure parameter. The resulting exponents for this case were very close to $2/3$: 0.66, 0.61, 0.69, and 0.65 for D_{LL} , D_{NN} , D_{WW} , and D_{TT} , respectively. This region will be referred to as the 3D scaling range. (The adjective “3D” is used to describe a range of scales for which the vertical velocity structure functions are on the same order as those of the horizontal velocities.)

Note that the D_{WW} curve in Fig. 3 exhibits a leveling off at scales above 1 km. This plateau shape is expected for separation distances much greater than the largest scale of the energy-containing eddies, with the plateau value equal to twice the variance of the signal (Monin and Yaglom 1975). For measurements that span a region much larger than the integral scale of the flow, structure functions should end in a plateau (referred to here as a terminal plateau). Structure functions that end with a nonzero slope indicate that sample regions are smaller than the largest scales; the D_{NN} and D_{TT} curves in Fig. 3 are examples of the latter. The shape of the D_{WW} curve in Fig. 3, including the hump preceding the plateau, can be generated by low-pass filtering data that does not exhibit a plateau, with the location of the hump related to the filter cutoff scale. Thus, the beginning of the plateau is an indirect measure of the largest scales.

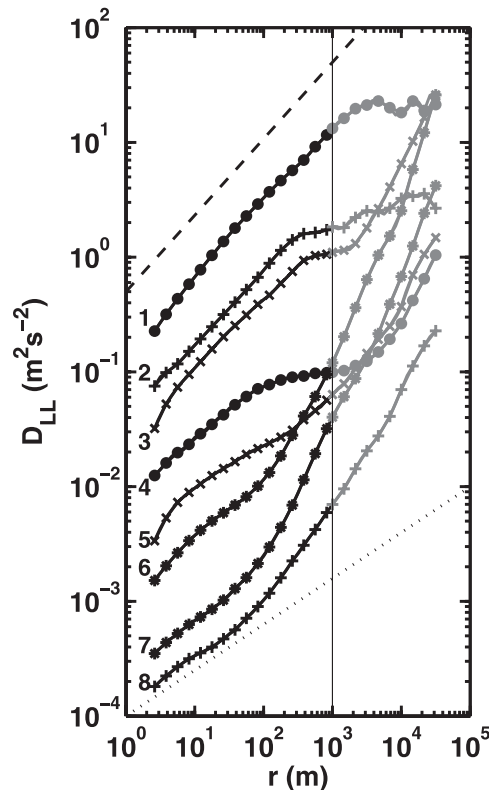


FIG. 4. Longitudinal velocity structure functions as a function of separation distance for eight individual flight segments: 1–6 Aug 1999, 9.7 km; 2–23 Aug 2001, 9.3 km; 3–6 Jun 2000, 11.4 km (Wales); 4–17 Aug 2001, 10.6 km; 5–10 May 2000, 12.3 km (Wales); 6–6 Jun 2000, 9.9 km (Wales); 7–26 Aug 1998, 6.6 km; 8–20 Feb 1999, 10.9 km (Japan). Dashed line shows $r^{2/3}$; dotted line shows $r^{2/5}$. Gray lines and symbols represent data at scales above aircraft inertia range.

The average structure functions for the individual flight segment were ensemble-averaged for all 129 levels and for various subensembles, weighted by the number of data points for each flight-segment average.

4. Results

a. Structure functions for individual segments

Longitudinal structure functions D_{LL} for eight individual level flight segments are shown in Fig. 4. Note that above 1 km, the curves are shown in gray to denote the region where aircraft trajectories are likely to influence scaling exponents. These cases were chosen to span the entire range of turbulence strength in the 3D scaling range, approximately evenly spaced. The strong turbulence cases (curves 1 through 3) all have extensive 3D scaling ranges, with scaling exponents close to $2/3$ (dashed line). In contrast, the weaker cases (curves 4 through 8) have smaller scaling ranges with exponents closer to 0.4 (dotted line). Only curve 1 displays a terminal plateau,

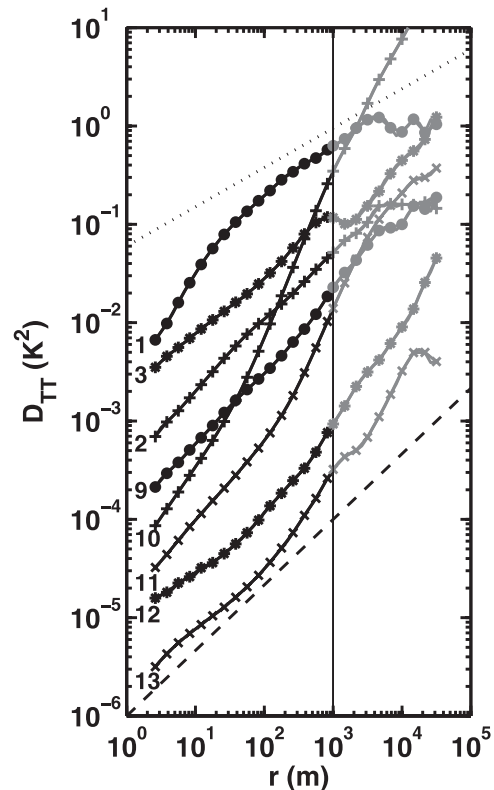


FIG. 5. Temperature structure functions as a function of separation distance for eight individual flight segments. Curves 1, 2, and 3, see Fig. 4; 9–26 Aug 1999, 12.5 km; 10–11 May 2000, 12.3 km (Wales); 11–18 May 2000, 13.8 km (Wales); 12–24 Aug 2001, 8.7 km; 13–6 Aug 1999, 12.2 km. Dashed line shows $r^{2/3}$; dotted line shows $r^{2/5}$. Gray lines and symbols represent data at scales above aircraft inertia range.

while curves 2 through 4 show a plateau level at intermediate scales (100 to 1000 m), followed by a subsequent increase in values at larger scales; this behavior indicates a distinct separation of small and large scales. The cases with weaker small-scale turbulence, curves 5 through 8, do not have a plateau level but instead display increasing slope above the shrinking 3D scaling range.

Temperature structure functions are shown in Fig. 5 for eight flight levels, with curves 1, 2, and 3 representing the same levels as those in Fig. 4. A striking feature is the wide range of slopes in the 3D scaling range. In addition, only curves 1 and 3 show plateaus, similar to their corresponding D_{LL} curves in Fig. 4. The rest of the cases display increasing slopes above the 3D scaling range.

A notable feature seen in Figs. 4 and 5 is the inconsistent relation between structure functions at small and large scales, best seen in curve 6 in Fig. 4 and curve 10 in Fig. 5. These both feature weak small-scale turbulence, but large-scale turbulence among the strongest of all cases. (See section 5a for more discussion).

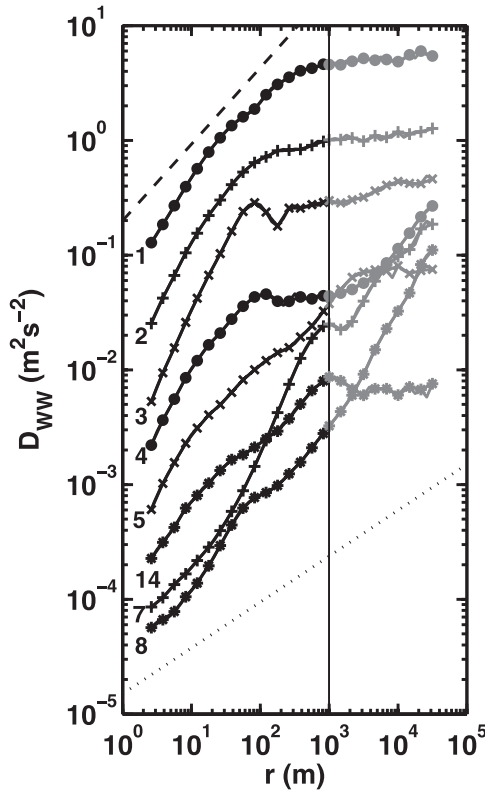


FIG. 6. Vertical velocity structure functions as a function of separation distance for eight individual flight segments. Curves 1–8, see Fig. 4; 14–12 Sep 2002, 10.4 km. Dashed line shows $r^{2/3}$; dotted line shows $r^{2/5}$. Gray lines and symbols represent data at scales above aircraft inertia range.

Figure 6 includes vertical velocity structure functions for eight individual segments, with all curves except for curve 14 representing the same flight levels as those in Fig. 4. With the exception of curve 8, all feature a plateau. The plateaus in curves 1 through 3 are terminal, while curve 4 displays an intermediate plateau. In curves 5, 14, and 7, the plateaus begin at kilometer scales, with no plateaus in the corresponding D_{LL} curve. Fifty-one of the 129 levels display some type of plateau.

Note that for curves 1 through 4, the plateaus begin at scales smaller than the plateaus in the corresponding D_{LL} curves (Fig. 4), indicating that limiting scales for the vertical fluctuations are smaller than those for the horizontal fluctuations. This suggests that the limiting scale for the vertical fluctuations is the vertical height of the CAT layer, an idea supported by the fact that the majority of the plateaus seen in D_{WW} begin at scales from 50 m to 1 km, echoing the range of UTLS CAT layer heights.

Plateaus are generally associated with the strongest turbulence, including the 20 levels with the strongest small-scale turbulence. It is not clear whether this connection

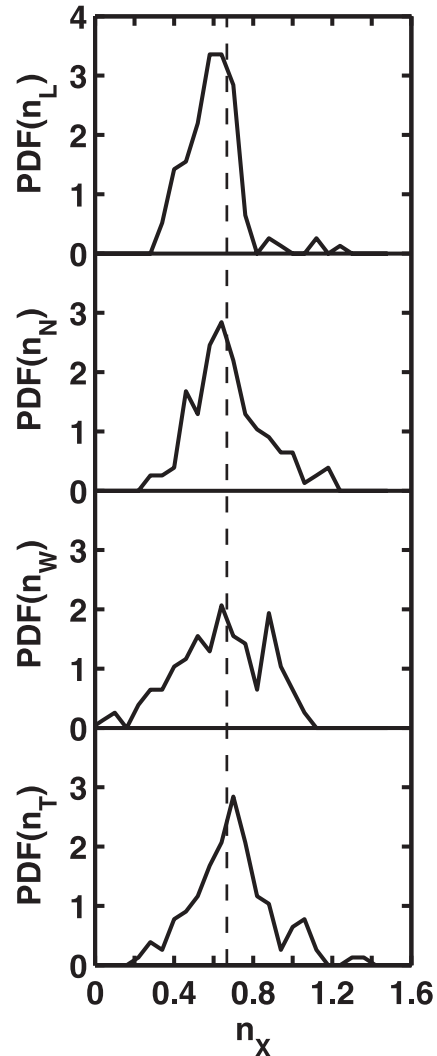


FIG. 7. Distributions of exponents n_X for velocity and temperature structure function; $D_{XX} \propto r^{n_X}$, where $X = L, T, W,$ or N . Vertical dashed line is $2/3$.

is rooted in physically relevant dynamics or is simply an indication that plateaus for weaker turbulence are masked by uncorrelated vertical motions. In the latter case, the presence or lack of a plateau is simply a consequence of the relative strengths of the small- and large-scale vertical motions.

b. Structure function scaling exponents and structure parameters

Distributions of the 3D scaling range structure function scaling exponents (e.g., n_L where $D_{LL} \propto r^{n_L}$) are shown in Fig. 7. All four distributions have peak values and mean values between 0.6 and 0.7, with mean values of 0.61 for n_L , 0.69 for n_N and n_T , and 0.62 for n_W . The n_L distribution has the narrowest distribution, with 90% of

the levels having an exponent between 0.4 and 0.75. The distributions for n_N and n_T are more symmetric and broader than that for n_L , while the n_W distribution is broader still with a secondary peak near 0.88. Although 79 of the 129 cases (61%) have values of n_L close to $2/3$ (0.55 to 0.8), only 21 of those have values of n_N , n_W , and n_T all within that range as well.

The range of values in structure function exponents for D_{LL} matches well with results of stratified-turbulence DNS from Werne and Fritts (2000); they report that the exponents for D_{LL} and D_{TT} concentrate between $2/5$ and $2/3$, with variations associated with location within the shear layer and the temporal development stage of the layer. This suggests that the range of structure function scaling exponents seen in the aircraft data may be a result of similar differences in the location and the time at which the CAT layers were sampled by the aircraft. However, further analysis of measured small-scale structure functions and direct numerical simulation (DNS) is needed to verify this. Although the $2/5$ value is a theoretical result for n_T in a buoyancy range (Bolgiano 1959), the corresponding value of $11/5$ for n_L was not seen in the DNS of Werne and Fritts (2000), nor is it evident in the experimental data reported here. As such, it would be erroneous to assume that the lower values are associated with buoyancy subrange scaling as described by Bolgiano (1959).

Even though there is a wide range of power-law exponents for the individual segments, the ensemble-averaged structure functions, for the overall ensemble and the subensembles, do feature exponents close to $2/3$ for all velocities and temperature (section 4c). This is qualitatively similar to observations by Duck and Whiteway (2005), who found that spectra for short, strong turbulence segments behaved as k^{-2} while averages of several segments fit well with $k^{-5/3}$. However, the range of scaling exponents seen here is likely not a short-segment effect, since no correlation is seen between segment length and scaling exponent for individual segments. In fact, the shortest level flight segment of 45.9 km, (which is still over 500 times longer than the end of the 3D scaling range) features n_L of 0.663, while for the longest flight segment, 386 km, $n_L = 0.54$. The reason that the ensemble averages have scaling exponents near $2/3$ is that the distributions of scaling exponents peak close to that value, so that most of the levels that make up the ensemble behave in that manner.

Figure 8a shows the distributions of structure parameters C_L^2 and C_T^2 , from the $r^{2/3}$ force-fits of D_{LL} and D_{TT} in the 3D scaling range (section 4a), using a \log_{10} bin size of 0.55. These follow a lognormal distribution (lines in the figure), a behavior predicted by Kolmogorov (1941) for dissipation and also shown by FS05. The upper scale in

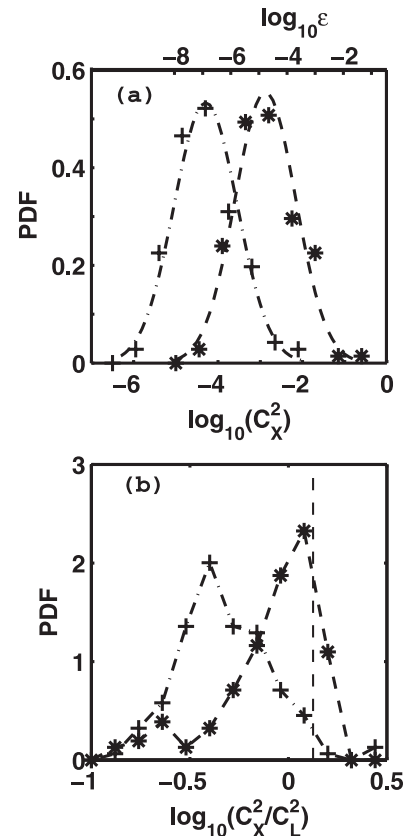


FIG. 8. (a) Distributions of C_L^2 ($\text{m}^{4/3} \text{s}^{-2}$) and C_T^2 ($\text{K}^2 \text{m}^{-2/3}$) for 3D scale range, using a \log_{10} bin size of 0.55; scale on upper axis is dissipation values corresponding to C_L^2 curve based on Eq. (4). Asterisks, C_L^2 ; crosses, C_T^2 ; dashed line, lognormal fit for C_L^2 ; dotted-dashed line, lognormal fit for C_T^2 . (b) Distributions of C_N^2/C_L^2 and C_W^2/C_L^2 for 3D scale range using a \log_{10} bin size of 0.12. Asterisks = C_N^2/C_L^2 ; crosses = C_W^2/C_L^2 ; vertical line marks isotropic value of $4/3$.

Fig. 8a indicates the dissipation values corresponding to the C_L^2 distribution based on Eq. (4). The means and standard deviations of the log distributions are as follows:

$$\begin{aligned} \langle \log_{10} C_L^2 \rangle &= -2.87; \quad \sigma_{\log_{10} C_L^2} = 0.719; \\ \langle C_L^2 \rangle &= 5.51 \times 10^{-3} \text{ m}^{4/3} \text{ s}^{-2}; \end{aligned} \quad (6)$$

$$\begin{aligned} \langle \log_{10} \epsilon \rangle &= -4.77; \quad \sigma_{\log_{10} \epsilon} = 1.08; \\ \langle \epsilon \rangle &= 3.57 \times 10^{-4} \text{ m}^2 \text{ s}^{-3}; \end{aligned} \quad (7)$$

$$\begin{aligned} \langle \log_{10} C_T^2 \rangle &= -4.29; \quad \sigma_{\log_{10} C_T^2} = 0.749; \\ \langle C_T^2 \rangle &= 2.77 \times 10^{-4} \text{ K}^2 \text{ m}^{-2/3}. \end{aligned} \quad (8)$$

The distributions of the structure parameters for the normal and vertical velocities are reported in Fig. 8b in the form of ratios against C_L^2 and are best matched by

a lognormal distribution. The peak of the log distribution for C_N^2/C_L^2 corresponds to a value of 1.2, close to the isotropic value of $4/3$. However, only 44 of the 129 levels display a value within $\pm 20\%$ of the isotropic value. The log distribution for C_W^2/C_L^2 exhibits greater deviation from isotropic values, centered on a peak corresponding to 0.40, and with only 3 of the 129 levels showing a value within $\pm 20\%$ of the isotropic value.

The significant variation of the lateral structure parameters from the isotropic value of $4/3$ may be an explanation for the wide range of scaling exponents seen in Fig. 7 (i.e., greater deviation from anisotropy may lead to scaling exponents farther from $2/3$). However, no correlation was observed between C_W^2/C_L^2 or C_N^2/C_L^2 and the scaling exponents for the individual levels.

Because of the wide range of scaling exponents shown in Fig. 7, the force-fit values of structure parameters should not be confused with the classic structure parameter defined for true $r^{2/3}$ scaling (i.e., the value of the structure function at $r = 1$ m). Rather, they represent a useful metric for comparing relative turbulence strengths in the 3D scaling range.

c. Ensemble-averaged structure functions and parameters

Ensemble-averaged structure functions for velocity and temperature as a function of separation distance are shown in Fig. 9, and the scaling exponents and structure parameters are included in column 1 of Table 2. The 3D scaling range for the velocity extends from 2 to 70 m, with exponents close to $2/3$ for D_{LL} and D_{NN} but larger for D_{WW} . The scaling range for temperature is between 100 and 1000 m, with an exponent of 0.7. Consistent with statistics of individual flight levels (Fig. 8), the normal and vertical velocity structure parameters reflect anisotropic behavior, with $C_N^2/C_L^2 = 0.88$ and $C_W^2/C_L^2 = 0.6$. At larger scales, greater than about 8 km, the power-law exponents of D_{LL} and D_{TT} range are between 0.75 and 0.85, although these values should be viewed with caution because of the small size of the linear range as well as the likely effect of aircraft trajectories at these scales (see section 2). At intermediate scales, D_{NN} and D_{LL} show a decreasing slope and D_{TT} an increasing slope, whereas D_{WW} diverges sharply from D_{LL} , the latter indicating a transition away from three-dimensional behavior.

Although the ensemble-averaged structure functions for all 129 levels are useful, they reveal only part of the picture because they are weighted heavily toward the strongest turbulence levels. To better study behavior for all turbulence levels, ensemble averages were found for three subensembles, with results shown in Fig. 10 and Table 2. The three subensembles for velocity structure functions are as follows:

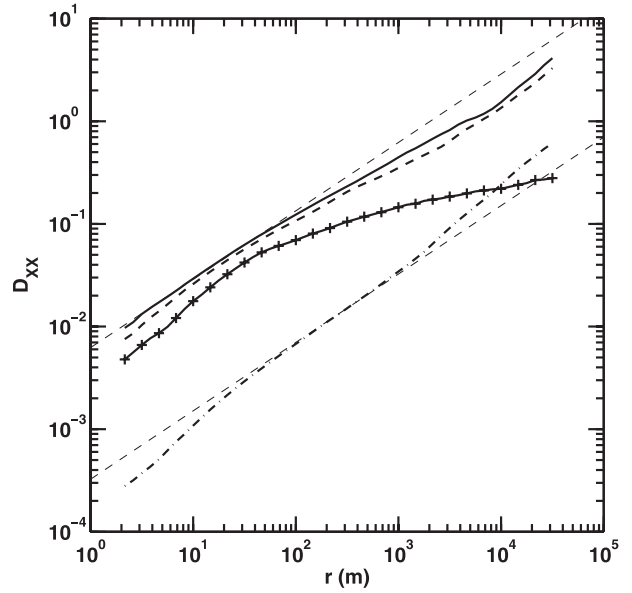


FIG. 9. Composite structure functions as a function of separation distance for all levels. Solid line: D_{LL} ($m^2 s^{-2}$); dashed line: D_{NN} ($m^2 s^{-2}$); solid line with plus symbols: D_{WW} ($m^2 s^{-2}$); dotted-dashed line: D_{TT} (K^2). Thin dashed lines: $r^{2/3}$.

- *Weak turbulence:* $[\log_{10} C_L^2 - \langle \log_{10} C_L^2 \rangle] < -\frac{1}{2} \sigma_{\log_{10} C_L^2}$ [see Eq. (6)],
- *Moderate turbulence:* $-\frac{1}{2} \sigma_{\log_{10} C_L^2} \leq [\log_{10} C_L^2 - \langle \log_{10} C_L^2 \rangle] < \frac{1}{2} \sigma_{\log_{10} C_L^2}$,
- *Strong turbulence:* $[\log_{10} C_L^2 - \langle \log_{10} C_L^2 \rangle] \geq \frac{1}{2} \sigma_{\log_{10} C_L^2}$.

Similar subensembles were defined for D_{TT} ensembles based on values of $\log_{10}(C_T^2)$.

For both D_{LL} and D_{TT} , the behavior at large scales is nearly the same for all ensembles, clearly illustrating the lack of correspondence between small- and large-scale values mentioned in section 4a. This suggests a “decoupling” of behavior in these two scale ranges. As such, the intermediate range scalings are mainly functions of the strength of the small-scale turbulence, with higher slopes for weaker turbulence. Following the trend seen in the overall ensemble averages, the 3D scaling range exponents are close to $2/3$ for the horizontal velocities and temperature, the exception being the weak turbulence ensemble with values for n_L , n_N , and n_W closer to 0.5. The ratio C_W^2/C_L^2 is approximately 0.6 for all ensembles, while C_N^2/C_L^2 varies between 0.82 and 1.0 with no apparent trend.

5. Discussion

The structure function data presented in section 4 revealed two important features that will be explored in more detail in this section—the decoupling of the small

TABLE 2. Structure parameters and isotropy ratios for ensemble-averaged structure functions.

$\log_{10}C_L^2$ range	All	>-2.52	-3.24 to -2.52	<-3.24
n_L	0.66	0.67	0.71	0.46
n_N	0.70	0.71	0.73	0.52
n_W	0.76	0.82	0.6	0.46
C_L^2 ($\text{m}^{4/3} \text{s}^{-2}$)	6.22×10^{-3}	1.85×10^{-2}	1.44×10^{-3}	3.17×10^{-4}
ε ($\text{m}^2 \text{s}^{-3}$)	1.73×10^{-4}	9.02×10^{-4}	1.93×10^{-5}	1.99×10^{-6}
C_N^2/C_L^2	0.88	0.87	1.00	0.82
C_W^2/C_L^2	0.60	0.61	0.64	0.62
$\log_{10}C_T^2$ range	ALL	>-3.92	-4.67 to -3.92	<-4.67
C_T^2 ($\text{K}^2 \text{m}^{-2/3}$)	3.25×10^{-4}	9.26×10^{-4}	6.54×10^{-5}	1.10×10^{-5}
n_T	0.70	0.78	0.67	0.67

and large scales, and the deviation of structure parameter from isotropic values. The focus will be on framing these small-scale behaviors in the context of 3D stratified shear turbulence. Such turbulence develops when the local Richardson number falls below a critical value because of high shear or weak stratification (Hazel 1972); the Richardson number is given by $\text{Ri} = N^2/S^2$, where S is the shear rate $\{=[(\partial u_L/\partial z)^2 + (\partial u_N/\partial z)^2]^{1/2}\}$ and N is the buoyancy frequency $\{=[g/\theta(\partial\theta/\partial z)]^{1/2}\}$ where θ is potential temperature.

Laboratory experiments (Miles 1961; Thorpe 1973a; DaSilva et al. 1996) have shown that the transition to turbulence is via the development of 2D Kelvin–Helmholtz (KH) billows that become unstable and eventually breakdown into 3D turbulence. Low Reynolds direct numerical simulations have provided additional insight into the evolution of stratified shear layer turbulence; these include the work of Smyth and Moum (2000), Smyth et al. (2001), Joseph et al. (2004), Palmer et al. (1994, 1996), and Werne and Fritts (1999, 2000).

The developing KH billow grows to a height larger than the initial shear-layer thickness. Shear layers with strong initial stability (i.e., larger Ri) result in thinner turbulence layers relative to the initial shear layer height, with vertical velocity levels and scales limited. The KH-to-turbulence transition process features several phases: 2D billow formation and rollup, initial transverse instability, transition to turbulence, and breakdown of the billow structure leading to a mainly parallel flow layer with decaying turbulence and internal gravity waves. Scaling and statistical characteristics vary among these phases and among different vertical locations within the layer (e.g., Smyth and Moum 2000; Smyth et al. 2001; Joseph et al. 2004). Unfortunately, these effects are difficult to capture with aircraft measurements, since there is no way to know the “age” of the layer or the vertical location within the layer.

Kelvin–Helmholtz instabilities are not the only possible source of the small-scale turbulence described here, but they will be the focus of the discussion in subsequent

sections. For other possible sources, see Whiteway et al. (2003a, 2004) and Duck and Whiteway (2005), who investigated gravity wave features of several of the flights reported here, and Riley and Lindborg (2008), who

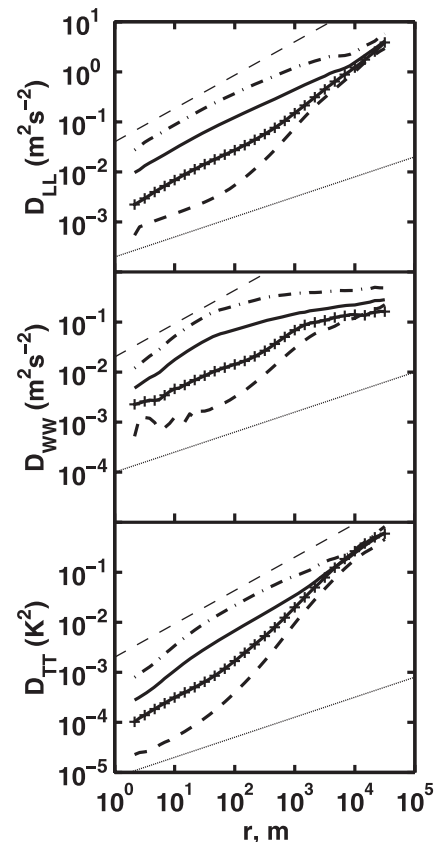


FIG. 10. Composite structure functions as a function of separation distance for subensembles of levels. Solid line, all levels (same as Fig. 9); dashed line, weak turbulence—all levels with $\log(C_L^2)$ or $\log(C_T^2) < 1/2\sigma$ below mean; solid line with plus symbols, moderate turbulence—all levels with $\log(C_L^2)$ or $\log(C_T^2)$ within $1/2\sigma$ of mean; dotted-dashed line, strong turbulence—all levels with $\log(C_L^2)$ or $\log(C_T^2) > 1/2\sigma$ above mean. Thin dashed lines show $r^{2/3}$; thin dotted line shows $r^{2/5}$.

proposed a model for stratified shear turbulence based on the breakup of large-scale horizontal motions.

a. Large- and small-scale decoupling

The notion of decoupling of small- and large-scale behavior refers to the fact that the strength of turbulence at large scales is not necessarily a good predictor of the strength at small scales. It is most evident in the individual level structure functions in Figs. 4–6 and the ensemble averages in Figs. 9 and 10. It can also be seen in the variety of scaling behavior in the intermediate scales (1 to 10 km) that may not necessarily represent any physically relevant mechanism but is simply a “bridge” between the two distinct scale ranges, adjusting to their relative strengths. Given this, extrapolation of large-scale behavior is a questionable approach for inferring small-scale turbulence, as proposed in FS05. The most striking evidence of decoupling is the plateau levels observed in D_{WW} ; clearly, vertical velocity is the best indicator of transition between 3D small-scale turbulence and large-scale motions dominated by horizontal velocities.

The source of energy for the small-scale turbulence seen in the aircraft measurements is at the scale of the most unstable wavelength of the initial shear instability, on the order of several kilometers. Larger-scale motions that may be present would not necessarily correlate with the stratified shear turbulence at smaller scales, leading to the decoupling seen in the structure functions. The lack of variability of the large-scale behavior, best seen in the ensemble-averaged D_{LL} and D_{TT} curves in Fig. 10, suggests that the mechanism responsible for these larger-scale motions may be more ubiquitous and uniform than those associated with the thin shear layers, which appear to be more intermittent and variable based on larger spread in the sub-kilometer structure functions. In essence, the large-scale motions develop independently from sub-kilometer-scale CAT layers. The exception to this would be situations for which the source of initial shear is connected to the large-scale motions; for example, Riley and Lindborg (2008) conjecture that energy injected at large horizontal scales could break down into smaller structures in the presence of strong stratification resulting in vertical shearing, development of 3D turbulence layers, and a downward cascade of energy.

For the majority of the 129 cases presented here, the jet stream is the likely source of the initial shear, since flight planning protocol focused on locating and targeting strong winds and shear associated with jet streams. The maximum jet stream speeds, based on atmospheric soundings at nearby locations (<http://weather.uwyo.edu/upperair/sounding.html>), were over 50 kt for 106 of the levels and over 90 kt for 98 levels. As a way to test the importance of the jet stream as a source of shear in the aircraft

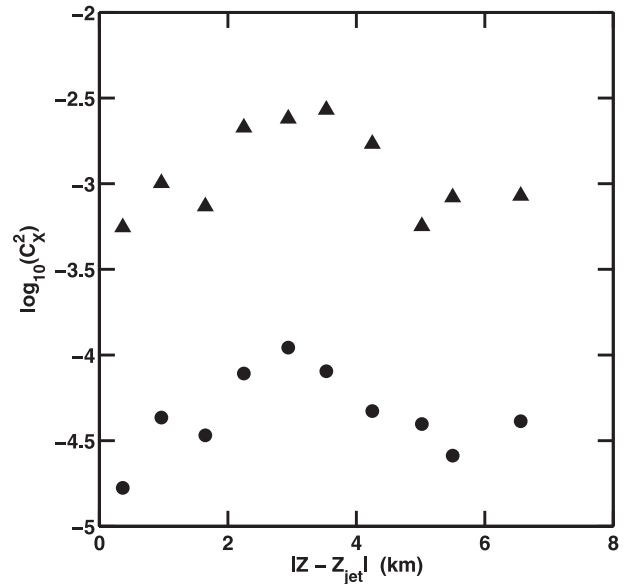


FIG. 11. The quantities C_L^2 ($\text{m}^{4/3} \text{s}^{-2}$) (triangles) and C_T^2 ($\text{K}^2 \text{m}^{-2/3}$) (circles) as a function of vertical distance from jet centerline $Z - Z_{\text{jet}}$. Values are averages over 0.65-m bins in $Z - Z_{\text{jet}}$.

measurements, the levels were binned based on absolute distance between the measured CAT level and the center of the jet found from the sounding profiles. As seen in Fig. 11, bin-averaged values of C_T^2 and C_L^2 (with bin sizes of 0.65 km) are highest at vertical locations between 2 and 4 km from the jet center, decreasing on either side, corresponding to high-shear regions along the wings of the jet.

The value of the structure functions at scales greater than about 5 km are likely contaminated by the trajectory–anisotropy effects discussed in section 2 (LST04; Lovejoy et al. 2009; Lilley et al. 2008). Although the analysis of such effects is not the focus of this paper, it is worth considering whether they are the source of the observed decoupling between small and large scales; that is, is the decoupling simply an artifact of aircraft measurements rather than a physical phenomenon rooted in the fluid dynamics of the atmosphere? Several points argue against that explanation, all based on the fact that any artifacts in the measurements due to the trajectory effects should appear at scales greater than about 1 km, the end of the range for which aircraft inertia smooths out trajectory effects. Figure 10 shows that the differences in turbulence strength that lead to the idea of decoupling occur at small scales, with the large-scale structure functions being nearly the same. Even if the large-scale behavior is primarily an artifact, it cannot explain the difference in turbulence levels at small scales. Along the same line, Lovejoy et al. (2009) showed that an initial “break” (change in scaling exponent) in the

spectra would occur at the end of the inertial range of the aircraft, but changes in slopes of the structure functions reported here occur at scales as low as tens of meters (see curves 7 and 8 on Fig. 4), well within the aircraft inertial range. In addition, Lovejoy et al. (2009) showed that temperature and humidity spectra did not display the same breaks as horizontal velocity, yet the decoupling effect and the changes in slope are seen here in temperature as well (seen most clearly in Fig. 10). Finally, the most obvious evidence of the decoupling is the plateau features of the vertical velocity structure function that signal a clear separation of scales; for all but 2 of the 51 cases that display such plateaus, these features begin well within the aircraft inertial region, as determined by the D_z data, and therefore cannot be explained as a trajectory-based artifacts.

b. Anisotropy¹

Despite the deviation of C_N^2 and C_W^2 from isotropic values of $\frac{1}{3}C_L^2$ in the 3D scaling range, the degree of anisotropy is relatively small in the sense that ratios of C_N^2/C_L^2 and C_W^2/C_L^2 are of $O(1)$. As such, estimates of dissipation found from Eq. (4) are probably reasonable in an order-of-magnitude sense, though further work is needed to quantify the extent to which this is true. The degree of anisotropy is larger in C_W^2 than in C_N^2 because of the effect of buoyancy, which suppresses vertical motions but not to the extent that the flow becomes two-dimensional. Gargett (1988) relates these two situations to the degree of stratification and would classify the weakly anisotropic condition seen here as “isotropic.”

The level of anisotropy in C_W^2 is correlated to the strength of the small-scale turbulence, with greater anisotropy for weaker turbulence cases. This is seen in the C_W^2/C_L^2 distributions in Fig. 12a for the weak and strong cases defined in section 4c, with the distribution peaking at 0.28 for the weak ensemble and 0.47 for the strong ensemble. Figure 12b further illustrates the anisotropy trend, showing bin-averaged values of C_W^2/C_L^2 increasing with increasing C_L^2 .

DNS and laboratory experiments of stratified shear turbulence have shown that Ri increases from its initial shear layer value as the layer develops, leveling off at values ranging from 0.25 to 0.4 during the latter phases of layer life when turbulence levels decay rapidly (Smyth and Moum 2000; Thorpe 1973b). These stronger levels of stratification give rise to internal gravity waves, and if the weaker turbulence cases reported here represent

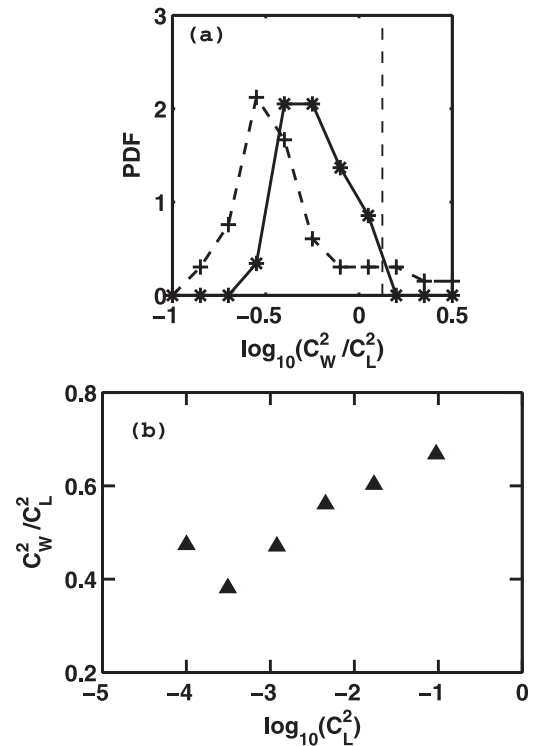


FIG. 12. (a) Distributions of ratio C_W^2/C_L^2 for 3D scale range using a \log_{10} bin size of 0.15. Asterisks indicate strong turbulence (see Fig. 10 caption); crosses, weak turbulence. Dashed vertical line represents isotropic value of $\frac{1}{3}$. (b) The ratio C_W^2/C_L^2 as a function of C_L^2 . Values are averages over bins of $\log_{10}(C_L^2)$, with a bin size of 0.6.

latter-stage shear layers, then their higher levels of anisotropy may also be a result of the stronger stratification. In support of this, structure function analysis of stratified-shear DNS revealed $C_W^2/C_L^2 = 0.43$ in the midlayer for the stage of evolution characterized by decaying turbulence (Werne and Fritts 2000). This value is close to those seen in Fig. 12b for the weakest turbulence cases.

6. Concluding remarks

High-resolution measurements obtained from a unique aircraft platform have shed light on turbulence behavior in the sub-kilometer range for which published data is scarce. At scales less than 100 m, structure functions exhibited power-law exponents that ranged from 0.4 to 0.75 for individual flight segments, but values close to $\frac{2}{3}$ for the overall ensemble and for various subensembles. Weakly anisotropic behavior was seen, with structure parameters C_N^2 and C_W^2 on the same order as C_L^2 but deviating from the expected isotropic value of $\frac{1}{3}C_L^2$. Anisotropy in C_W^2 was stronger on average for weaker turbulence levels, consistent with DNS findings. This 3D subrange was decoupled from behavior at scales greater

¹ Note that anisotropy here refers to deviation of structure parameters from the isotropic values and is not an indication of anisotropic scaling as described by Lovejoy et al. (2007).

than 10 km, which exhibited less variation in the structure function values, suggesting that mechanisms associated with small-scale stratified shear turbulence are more intermittent and variable than those associated with large-scale behavior. The observed decoupling calls into question the use of mesoscale data to infer microscale behavior. The D_{WW} curves displayed plateau levels characteristic of a limiting vertical scale, a feature generally associated with stronger turbulence levels in the 3D scaling range.

Acknowledgments. The authors acknowledge the continued support of Dr. Arje Nachman of AFOSR. DEW was supported by the National Research Council, through the Air Force Summer Faculty Fellowship and Senior Research Associateship programs. Special acknowledgment goes to the late Timothy Crawford of NOAA who designed and built the turbulence probes and who championed the use of small aircraft for studying big turbulence issues. Thanks to Joe Werne, Colorado Research Associates, Northwest Research Associates, for kindly providing his unpublished DNS results and for his input and discussions regarding Kelvin–Helmholtz layer development. The authors are also grateful to the reviewers for their insightful and very useful comments and suggestions.

REFERENCES

- Antonia, R. A., and R. J. Smalley, 2001: Scaling range exponents from X-wire measurements in the atmospheric surface layer. *Bound.-Layer Meteor.*, **100**, 439–457.
- Bolgiano, R., 1959: Turbulent spectra in a stably stratified atmosphere. *J. Geophys. Res.*, **64**, 2226–2229.
- Chan, K. R., J. Dean-Day, S. W. Bowen, and T. P. Bui, 1998: Turbulence measurements by the DC-8 Meteorological Measurement System. *Geophys. Res. Lett.*, **25**, 1355–1358.
- Cho, J. Y. N., and E. Lindborg, 2001: Horizontal velocity structure functions in the upper troposphere and lower stratosphere. 1. Observation. *J. Geophys. Res.*, **106** (D10), 10 223–10 232.
- Crawford, T. L., and R. J. Dobosy, 1992: A sensitive fast-response probe to measure turbulence and heat flux from any airplane. *Bound.-Layer Meteor.*, **59**, 257–278.
- , and —, 1997: Pieces to a puzzle: Air-surface exchange and climate. *GPS World*, **8** (11), 32–39.
- DaSilva, I. P. D., J. S. Fernando, F. Eaton, and D. Hebert, 1996: Evolution of Kelvin–Helmholtz billows in nature and laboratory. *Earth Planet. Sci. Lett.*, **143**, 217–231.
- Duck, T. J., and J. A. Whiteway, 2005: The spectrum of waves and turbulence in the tropopause. *Geophys. Res. Lett.*, **32**, L07801, doi:10.1029/2004GL021189.
- Frehlich, R., and R. Sharman, 2005: Estimates of turbulence from numerical weather prediction model output with applications to turbulence diagnosis and data assimilation. *Mon. Wea. Rev.*, **132**, 2308–2324.
- Gargett, A. E., 1988: The scaling of turbulence in the presence of stable stratification. *J. Geophys. Res.*, **93** (C5), 5021–5036.
- Garman, K. E., and Coauthors, 2006: An airborne and wind tunnel evaluation of a wind turbulence measurement system for aircraft-based flux measurements. *J. Atmos. Oceanic Technol.*, **23**, 1696–1708.
- Hazel, P., 1972: Numerical studies of the stability of inviscid stratified shear flows. *J. Fluid Mech.*, **51**, 39–61.
- Jaspersion, W. H., G. D. Nastrom, and D. C. Fritts, 1990: Further study of terrain effects on the mesoscale spectrum of atmospheric motions. *J. Atmos. Sci.*, **47**, 979–987.
- Joseph, B., A. Mahalov, B. Nicolaenko, and K. L. Tse, 2004: Variability of turbulence and its outer scales in a model tropopause jet. *J. Atmos. Sci.*, **61**, 621–643.
- Kennedy, P. J., and N. A. Shapiro, 1980: Further encounters with clear air turbulence in research aircraft. *J. Atmos. Sci.*, **37**, 986–993.
- Kolmogorov, A. N., 1941: The local structure of turbulence in incompressible viscous fluid for very large Reynolds numbers. *Dokl. Akad. Nauk SSSR*, **30**, 9–13.
- Lilley, M., S. Lovejoy, K. B. Strawbridge, D. Schertzer, and A. Radkevich, 2008: Scaling turbulent atmospheric stratification. II: Spatial stratification and intermittency from lidar data. *Quart. J. Roy. Meteor. Soc.*, **134**, 301–315.
- Lindborg, E., 1999: Can the atmospheric kinetic energy spectrum be explained by two-dimensional turbulence? *J. Fluid Mech.*, **388**, 259–288.
- Lovejoy, S., D. Schertzer, and A. F. Tuck, 2004: Fractal aircraft trajectories and nonclassical turbulent exponents. *Phys. Rev. E*, **70**, 036306, doi:10.1103/PhysRevE.70.036306.
- , A. F. Tuck, S. J. Hovde, and D. Schertzer, 2007: Is isotropic turbulence relevant in the atmosphere? *Geophys. Res. Lett.*, **34**, L15802, doi:10.1029/2007GL029359.
- , —, D. Schertzer, and S. J. Hovde, 2009: Reinterpreting aircraft measurements in anisotropic scaling turbulence. *Atmos. Chem. Phys. Discuss.*, **9**, 3871–3920.
- Marengo, A., and Coauthors, 1998: Measurement of ozone and water vapor by Airbus in-service aircraft: The MOZAIC airborne program, an overview. *J. Geophys. Res.*, **103**, 25 631–25 642.
- Miles, J. W., 1961: On the stability of heterogeneous shear flows. *J. Fluid Mech.*, **10**, 496–508.
- Monin, A. S., and A. M. Yaglom, 1975: *Statistical Fluid Mechanics*. MIT Press, 886 pp.
- Nastrom, G. D., and W. H. Jaspersion, 1983: Flight summaries and temperature climatology at airliner cruise altitudes from GASP (Global Atmospheric Sampling Program) data. NASA Rep. CR-168106, 368 pp.
- , and K. S. Gage, 1985: A climatology of atmospheric wave-number spectra of wind and temperature observed by commercial aircraft. *J. Atmos. Sci.*, **42**, 950–960.
- , —, and W. H. Jaspersion, 1984: Kinetic energy spectrum of large- and mesoscale atmospheric processes. *Nature*, **310**, 36–38.
- Nichols-Pagel, G. A., D. B. Percival, P. G. Reinhall, and J. J. Riley, 2008: Should structure functions be used to estimate power laws in turbulence? A comparative study. *Physica D*, **237**, 665–677.
- Palmer, T. L., D. C. Fritts, Ø. Andreassen, and I. Lie, 1994: Three-dimensional evolution of Kelvin–Helmholtz billows in stratified compressible flow. *Geophys. Res. Lett.*, **21**, 2287–2290.
- , —, and —, 1996: Evolution and breakdown of Kelvin–Helmholtz billows in stratified compressible flows. Part II: Instability structure, evolution and energetics. *J. Atmos. Sci.*, **53**, 3192–3212.

- Perkins, P. J., 1976: Global measurements of gaseous and aerosol trace species in the upper troposphere and lower stratosphere from daily flights of 747 airliners. NASA-TMX-73544, 18 pp.
- Riley, J., and E. Lindborg, 2008: Stratified turbulence: A possible interpretation of some geophysical turbulence measurements. *J. Atmos. Sci.*, **65**, 2416–2424.
- Smyth, W. D., and J. M. Moum, 2000: Length scales of turbulence in stably stratified mixing layers. *Phys. Fluids*, **12**, 1327–1342.
- , —, and D. R. Caldwell, 2001: The efficiency of mixing in turbulent patches: Inferences from direct simulations and microstructure observations. *J. Phys. Oceanogr.*, **31**, 1969–1992.
- Thorpe, S. A., 1973a: Experiments on instability and turbulence in a stratified shear flow. *J. Fluid Mech.*, **61**, 731–751.
- , 1973b: Turbulence in stably stratified fluids: A review of laboratory experiments. *Bound.-Layer Meteor.*, **5**, 95–119.
- Werne, J., and D. C. Fritts, 1999: Stratified shear turbulence: Evolution and statistics. *Geophys. Res. Lett.*, **26**, 439–442.
- , and —, 2000: Structure functions in stratified shear turbulence. *10th DoD HPC User Group Conf.*, Albuquerque, NM, Department of Defense, 1–11.
- Whiteway, J. A., E. G. Pavelin, R. Busen, J. Hacker, and S. Vosper, 2003a: Airborne measurements of gravity wave breaking at the tropopause. *Geophys. Res. Lett.*, **30**, 2070, doi:10.1029/2003GL018207.
- , and Coauthors, 2003b: Results from Emerald-2: Measurements in the cirrus outflow from tropical convection above Darwin. *Proc. AGU Fall Meeting*, San Francisco, CA, Amer. Geophys. Union, A12D-04.
- , G. P. Klaassen, N. G. Bradshaw, and J. Hacker, 2004: Transition to turbulence in shear above the tropopause. *Geophys. Res. Lett.*, **31**, L02118, doi:10.1029/2003GL018509.
- Wyngaard, J. C., and O. R. Coté, 1971: The budgets of turbulent kinetic energy and temperature variance in the atmospheric surface layer. *J. Atmos. Sci.*, **28**, 190–201.